Fast damage imaging using the time-reversal technique in the frequency–wavenumber domain

2013 Smart Mater. Struct. 22 075028

(http://iopscience.iop.org/0964-1726/22/7/075028)

IOP Publishing Smart Materials and Structures
Smart Mater. Struct. **22** (2013) 075028 (11pp) doi:10.1088/0964-1726/22/7/075028

Fast damage imaging using the time-reversal technique in the frequency–wavenumber domain

R Zhu[1], G L Huang[1] and F G Yuan[2]

[1] Department of Systems Engineering, University of Arkansas at Little Rock, Little Rock, AR 72204, USA
[2] Department of Mechanical and Aerospace Engineering, North Carolina State University, Raleigh, NC 27695, USA

E-mail: glhuang@ualr.edu and yuan@ncsu.edu

Received 26 January 2013, in final form 14 May 2013
Published 21 June 2013
Online at stacks.iop.org/SMS/22/075028

Abstract
The time-reversal technique has been successfully used in structural health monitoring (SHM) for quantitative imaging of damage. However, the technique is very time-consuming when it is implemented in the time domain. In this paper, we study the technique in the frequency–wavenumber (f–k) domain for fast real-time imaging of multiple damage sites in plates using scattered flexural plate waves. Based on Mindlin plate theory, the time reversibility of dispersive flexural waves in an isotropic plate is theoretically investigated in the f–k domain. A fast damage imaging technique is developed by using the cross-correlation between the back-propagated scattered wavefield and the incident wavefield in the frequency domain. Numerical simulations demonstrate that the proposed technique cannot only localize multiple damage sites but also potentially identify their sizes. Moreover, the time-reversal technique in the f–k domain is about two orders of magnitude faster than the method in the time domain. Finally, experimental testing of an on-line SHM system with a sparse piezoelectric sensor array is conducted for fast multiple damage identification using the proposed technique.

(Some figures may appear in colour only in the online journal)

1. Introduction

Increasing emphasis on the integrity of critical structures such as aircraft, civil infrastructure, nuclear reactors, pressure vessels, and so on, creates an urgent need to monitor structures *in situ* and in real-time and detect damage at an early stage to prevent catastrophic failure [1]. Recent advances in sensing technologies along with current developments in computation and communications have resulted in a significant interest in developing structural health monitoring (SHM) technologies that can be integrated seamlessly into the structures as a built-in diagnosis system [2–4]. Using distributed sensors to monitor the physical condition of in-service structures becomes feasible if sensor signals can be interpreted accurately and rapidly to reflect the *in situ* condition of the structures through real-time data processing [5].

In general, the algorithms used in a built-in SHM system can be mainly classified into vibration-based and wave-based approaches [3, 4]. Though the vibration-based method seems to be an intuitive way to detect damage, i.e., changes of modal parameters indicate a change in the physical condition of the structure, the major challenge with the vibration-based method is that it is relatively insensitive to local damage compared with other likely changes in the structure or its surroundings, such as changes in temperature or boundary conditions. Therefore it cannot localize and identify small damage sites accurately [4]. In contrast, the wave-based method can extract the damage information contained in the transient stress waves transmitting in the structure, and is

considered as a promising technique to detect small local damage in plate-like structures, especially for large-area structures, such as wings and fuselages [6]. A wide range of theoretical and experimental studies have been performed to assess the effectiveness and efficacy of damage identification in plate-like structures using Lamb waves [7–13]. However, their dispersive nature and the existence of many modes simultaneously can complicate the interpretation of the acquired signal.

Signal processing and damage imaging techniques are of primary importance in establishing any Lamb wave-based SHM. Different imaging approaches have been proposed for the detection of damage in structures based on the propagation of guided waves and the measurement of reflections induced by damage. For example, Giurgiutiu and Bao [14] and Yu and Giurgiutiu [15] developed an 'embedded ultrasonic structural radar' (EUSR) algorithm using a linear phased array of piezoelectric elements. With the virtual beam formation and focusing, no physical manipulation of the transducers is needed and both the excitation signal and received signal are boosted several times; therefore the signal-to-noise ratio (SNR) is increased. However, the large number of data points in each signal made the process very time-consuming. Quaegebeur *et al* [16] and Raghavan and Cesnik [17] have successfully used time-domain correlation of the signals and time of flight (TOF) imaging for pulse-echo based damage detection and characterization. The methods showed good performance in detecting the locations of simulated cracks or corrosion. However, those imaging techniques cannot provide accurate quantitative information about the monitored damage, such as the shape and size.

The time-reversal technique has been introduced in SHM to compensate for the dispersion of plate waves and quantitatively detect defects with improved SNR and spatial resolution [18]. Also, the time-reversal method has been used to focus Lamb wave energy to detect flaws or damage in plates [19]. Sohn *et al* [20–22] advanced the time-reversal process concept to develop a SHM technique where defects can be identified without requiring direct comparison with previously obtained baseline data. Wang and Huang [23] applied the reverse wave method to identify cracks embedded in plane elastic media based on surface signals. Images of different embedded cracks are obtained based on both incident longitudinal and shear waves. Lin and Yuan [24–26] performed a systematic investigation of built-in piezoelectric SHM using a time-reversal method to visualize incipient damage in isotropic plates. The results of both numerical simulations and experimental studies demonstrated that the time-reversal method possesses the capability to identify multiple discrete damage without *a priori* assumptions on the distributed pattern of the damage. It is noticed that either the finite element (FE) method or the finite difference (FD) method was employed to perform the reverse wave propagation in the above-mentioned literature. Therefore, very dense discretization in the spatial and time domains is required to guarantee numerical stability and minimize grid dispersion due to the small wavelength of the stress wave employed at high frequency, which significantly increases the computation time and limits applications of the time-reversal technique in real-time SHM.

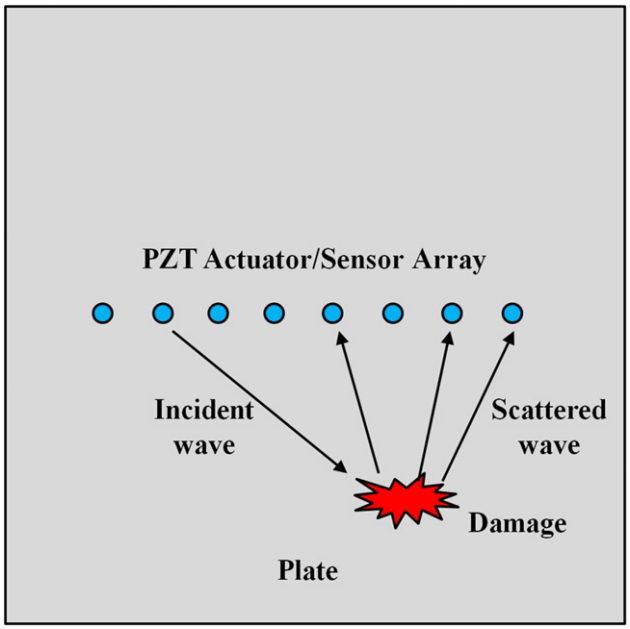

Figure 1. Illustration of the time-reversal process for damage identification.

In order to provide a computationally efficient solution for fast and real-time damage detection, we propose a time-reversal technique in the frequency–wavenumber (f–k) domain using scattered flexural plate waves. First, the basic idea of damage detection using the time-reversal technique is described and the formulation of the first mode of the flexural wave in the f–k domain is analytically developed based on Mindlin plate theory. Then, a cross-correlation imaging condition is introduced in the frequency domain. Numerical simulations are performed to validate the proposed technique and imaging condition to identify damage by back-propagating the synthetic scattered wavefields toward the damage in the frequency domain. Finally, experimental testing is conducted to confirm that the proposed technique can be a powerful tool for quantitatively visualizing damage in an on-line SHM system with a sparse sensor array.

2. Time-reversal technique in the f–k domain for damage imaging

2.1. Time-reversal process of flexural plate waves in the f–k domain

Figure 1 illustrates a plate with a piezoelectric lead zirconate titanate (PZT) array bonded on its surface. These PZT wafers act as actuators and sensors alternately. When a diagnostic wave excited by an actuator propagating in the structure encounters the damage, part of the wave will be reflected by the damage in all directions, known as scattering. Each time an actuator is actuated and sends out a transient wave, each sensor will record a trace of the scattered waves. A time section of the recorded waves is obtained by presenting the

traces from all the sensors for the same shot. The final target is to identify the location and the extent of the damage from the recorded waves.

With the ability to separate individual wave modes in the f–k domain, the direction- and frequency-dependent wave propagation and scattering behavior can be measured and utilized for imaging damage. The technique through the analysis of the full wavefield in the f–k domain was presented as an effective tool for damage detection, visualization and characterization [27]. An *et al* [28] presented an image processing technique in the f–k domain to isolate and visualize crack-induced standing wave energy from the constructed ultrasonic propagation images. However, the image formation from those approaches usually requires the extensive measured wavefield covered in the monitored area.

In the time-reversal process, the recorded waves are treated as excitations and used to reconstruct the spatial wavefield between the damage and the sensor array. The inverse process deals with back-propagating the linear array recorded waves to obtain secondary sources by systematically solving the wave equations as time-dependent boundary value problems based on Huygens' principle. In this study, to clearly illustrate this concept, by solving the flexural wave equation based on Mindlin plate theory in the f–k domain, the computational efficiency could be significantly increased. It should be emphasized that this method can be easily extended to consider multiple wave modes in the f–k domain without any difficulty.

Considering a two-dimensional isotropic plate as shown in figure 1, taking rotary inertia and the shear effect into account, the governing equation describing flexural waves based on Mindlin plate theory can be written as [29]

$$\left(\nabla^2 - \frac{\rho}{\kappa^2 G}\frac{\partial^2}{\partial t^2}\right)\left(D\nabla^2 - \frac{\rho h^3}{12}\frac{\partial^2}{\partial t^2}\right) w(x, y, t) + \rho h \frac{\partial^2 w(x, y, t)}{\partial t^2} = 0 \tag{1}$$

where $w(x, y, t)$ is the out-of-plane displacement, $\nabla^2 = \frac{\partial^2}{\partial x^2} + \frac{\partial^2}{\partial y^2}$ is the Laplacian operator and the shear correction factor is chosen as $\kappa = \pi/\sqrt{12}$ [30].

Applying the temporal Fourier transform to equation (1), yields

$$(\nabla^4 + A\nabla^2 + B)W(x, y, \omega) = 0 \tag{2}$$

where $A = (\frac{\rho h^3}{12D} + \frac{\rho}{\kappa^2 G})\omega^2$, $B = (\frac{\rho^2 h^3}{12\kappa^2 GD}\omega^2 - \frac{\rho h}{D})\omega^2$ and $W(x, y, \omega)$, with the argument ω simply represented as the Fourier transform of $w(x, y, t)$ with time variable t:

$$W(x, y, \omega) = \int_{-\infty}^{\infty} w(x, y, t)\mathrm{e}^{-\mathrm{i}\omega t}\,\mathrm{d}t \tag{3a}$$

$$w(x, y, t) = \frac{1}{2\pi}\int_{-\infty}^{\infty} W(x, y, \omega)\mathrm{e}^{\mathrm{i}\omega t}\,\mathrm{d}\omega. \tag{3b}$$

Equation (2) can be written as two Helmholtz equations:

$$(\nabla^2 + k_1^2)W(x, y, \omega) = 0 \tag{4a}$$

$$(\nabla^2 - k_2^2)W(x, y, \omega) = 0 \tag{4b}$$

where $k_1^2 = (\sqrt{A^2 - 4B} + A)/2$ and $k_2^2 = (\sqrt{A^2 - 4B} - A)/2$. k_1 and k_2 are wavenumbers corresponding to the first and second mode of the flexural waves, respectively.

Below the cut-off frequency of the second flexural wave $\omega_{\text{cut-off}} = \sqrt{12\kappa^2 G/\rho h^2}$, equation (4*a*) describes the traveling wave and equation (4*b*) describes the evanescent wave [30]. Let a linear array of sensors be located along the horizontal axis. Considering only the outgoing wave in equation (4*a*) and applying the spatial Fourier transform to $w(x, y, \omega)$ with respect to x, we have:

$$\bar{W}(k_x, y, \omega) = \int_{-\infty}^{\infty} W(x, y, \omega)\mathrm{e}^{\mathrm{i}k_x x}\,\mathrm{d}x = \int_{-\infty}^{\infty}\int_{-\infty}^{\infty} w(x, y, t)\mathrm{e}^{\mathrm{i}(k_x x - \omega t)}\,\mathrm{d}x\,\mathrm{d}t. \tag{5a}$$

The inverse Fourier transform of equation (5*a*) gives

$$w(x, y, t) = \frac{1}{4\pi^2}\int_{-\infty}^{\infty}\int_{-\infty}^{\infty} \bar{W}(k_x, y, \omega)\mathrm{e}^{-\mathrm{i}(k_x x - \omega t)}\,\mathrm{d}k_x\,\mathrm{d}\omega \tag{5b}$$

where $k_x = k\cos\theta$ is the component of k in the x-direction and θ is the angle between the x axis and the propagation direction. Here, for convenience, k_1 in equation (4*a*) is replaced by k. In equation (5*b*), $\bar{W}(k_x, y, \omega)$ can be regarded as a two-dimensional Fourier transform of $w(x, y, t)$ with respect to x and t. Accordingly, using equation (5*a*), equation (4*a*) is transformed to

$$\frac{\partial^2 \bar{W}(k_x, y, \omega)}{\partial y^2} = -(k^2 - k_x^2)\bar{W}(k_x, y, \omega) = -k_y^2 \bar{W}(k_x, y, \omega) \tag{6}$$

where $k_y = k\sin\theta$ is the component of k in the y-direction. The solution of equation (6) is

$$\bar{W}(k_x, y, \omega) = (C_1\mathrm{e}^{\mathrm{i}k_y y} + C_2\mathrm{e}^{-\mathrm{i}k_y y})\mathrm{e}^{\mathrm{i}\omega t} \tag{7}$$

where C_1 and C_2 are constants to be determined by the boundary conditions. Considering only the up going wave from the damage to the sensor array, which is the first term in the right hand side of equation (7), replacing C_1 by C and omitting the harmonic wave term $\mathrm{e}^{\mathrm{i}\omega t}$, it yields

$$\bar{W}(k_x, y, \omega) = C\mathrm{e}^{\mathrm{i}k_y y}. \tag{8}$$

When $y = 0$,

$$C = \bar{W}^{\mathrm{s}}(k_x, 0, \omega) \tag{9}$$

which is the two-dimensional Fourier transform of the recorded scattered wavefield $w^{\mathrm{s}}(x, y, t)$ at $y = 0$ received by the sensors. The superscript 's' represents the scattered wavefield. It should be mentioned that the strain field will be measured when the piezoelectric sensors are used. However, for the current linear problem, the time-reversal implementation based on the displacement field will not affect the final conclusion, which will also be validated in the following experimental testing. It is also assumed that the sensors are perfectly mounted on the plate and are sufficiently small such that the scattering effect of the sensor on the

received waves is also neglected in current study. Thus equation (8) can be written as

$$\bar{W}^{s}(k_x, y, \omega) = \bar{W}^{s}(k_x, 0, \omega)e^{ik_y y}. \quad (10)$$

Inverting equation (10) into the spatial domain yields

$$W^{s}(x, y, \omega) = \frac{1}{2\pi}\int_{-\infty}^{\infty} \bar{W}^{s}(k_x, 0, \omega)e^{ik_y y}e^{-ik_x x}\,dk_x. \quad (11)$$

Equation (11) is an important formulation for the time-reversal process of the first mode of the flexural wave in the f–k domain. It represents the back-propagated scattered wavefield in the frequency domain. The reverse wavefield in the time domain, i.e. $w^{s}(x, y, t)$, can be simply obtained by performing an inverse temporal Fourier transform on $W^{s}(x, y, \omega)$.

One major difference of damage detection using a flexural plate wave rather thanan acoustic wave is the inherent dispersive nature of the plate wave. By using the discrete digital signal processing method, equation (11) can be conveniently solved with known dispersion relationships. At every discrete point (x_m, y_n) $(m = 1, 2, \ldots, M;\ n = 1, 2, \ldots, N; M$ and N are the numbers of discrete points in x- and y-direction, respectively), by using the wavenumber–frequency dispersion relationship of the first mode of the flexural plate wave, the scattered wavefield recorded by the sensor array at $y = 0$ can be back-propagated to any (x_m, y_n) in the plate.

2.2. Cross-correlation imaging condition

Computation of the imaging condition is the key to the time-reversal damage detection technique. The time-reversal process of the scattered wavefield allows the scattered wave to propagate back toward the secondary sources, i.e., the damage. However, for damage imaging, the locations and extent of the damage are unknown during this process. When and where should the back-propagating scattered wavefield end to illuminate the damage? The answer can be given by the imaging condition. In this study, a cross-correlation imaging condition is employed in the frequency domain. The key idea by which the imaging condition is defined is based on the concept that the damage exists at places where the back-propagated scattered wave and the incident wave are in phase. In practice, the image can be visualized by taking the zero lag cross-correlation value of the two wavefields as the pixel value at each discrete point (x_m, y_n) [31].

$$I(x_m, y_n) = \sum_{\omega} W^{i}(x_m, y_n, \omega)W^{s*}(x_m, y_n, \omega) \quad (12)$$

where $I(x_m, y_n)$ is the zero lag cross-correlation value at a discrete pixel point $(x_m,\ y_n)$, and $W^{i}(x_m, y_n, \omega)$ and $W^{s}(x_m, y_n, \omega)$ are the back-propagated incident and scattered wavefields at (x_m, y_n) in the frequency domain, respectively. The superscripts 'i' and 's' represent the incident wavefield and the scattered wavefield, respectively. The superscript '$*$' represents the complex conjugate. As a result, the cross-correlation value will be relatively large at the damage domain, while it will be small or near zero at other places. Thus, the damage can be visualized by displaying the pixel values in a color map, indicating the damage sites with highlighted image intensity. Theoretically, the frequency-domain multiplication imaging technique made at multiple frequencies and the time-domain correlation imaging technique [23] sampled at multiple times will provide the same damage information. A frequency-domain system requires the summation of images from multiple frequencies and a time-domain system requires adding images taken at a number of times to achieve acceptable damage images.

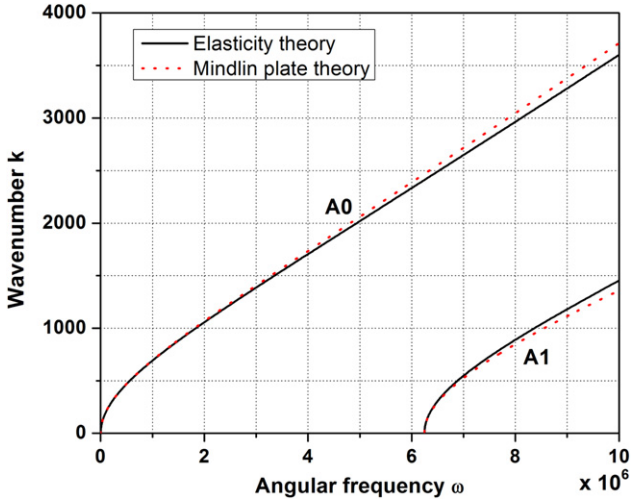

Figure 2. Dispersion curves of antisymmetric Lamb waves from Mindlin plate theory and elasticity theory.

3. Numerical results

3.1. Generation of synthetic scattered wavefields and incident wavefields

To illustrate the effectiveness and efficiency of the proposed damage detection method using the time-reversal technique in the f–k domain, numerical studies on an isotropic plate are performed. A square aluminum plate with $h = 1.6$ mm, $E = 72$ GPa, $\nu = 0.3$ and $\rho = 2730$ kg m^{-3} is considered. Figure 2 shows the dispersion curves of the antisymmetric waves of the first (A_0) and second (A_1) modes in the plate obtained from both the exact elastic Rayleigh–Lamb equation and Mindlin plate theory. In the figure, ω is the angular frequency and k is the wavenumber. Notice that $\omega = 6.25 \times 10^6$ s^{-1} is the cut-off angular frequency of the second flexural wave mode. It can be found that for the first flexural wave mode, the result from Mindlin plate theory agrees very well with that given by exact elasticity theory, demonstrating the rationale of using Mindlin plate theory.

For simulating direct and scattered wave propagation in plate structures, a MacCormack 2–6 order explicit FD method developed by Lin and Yuan [24, 25] is employed to obtain the synthetic scattered out-of-plane wavefields from the damage, which will be used as sensor signals in the reversal wave technique. The details of this explicit FD method can be found in the corresponding literature, and therefore are not repeated here. In the FD method, each damage point is modeled as

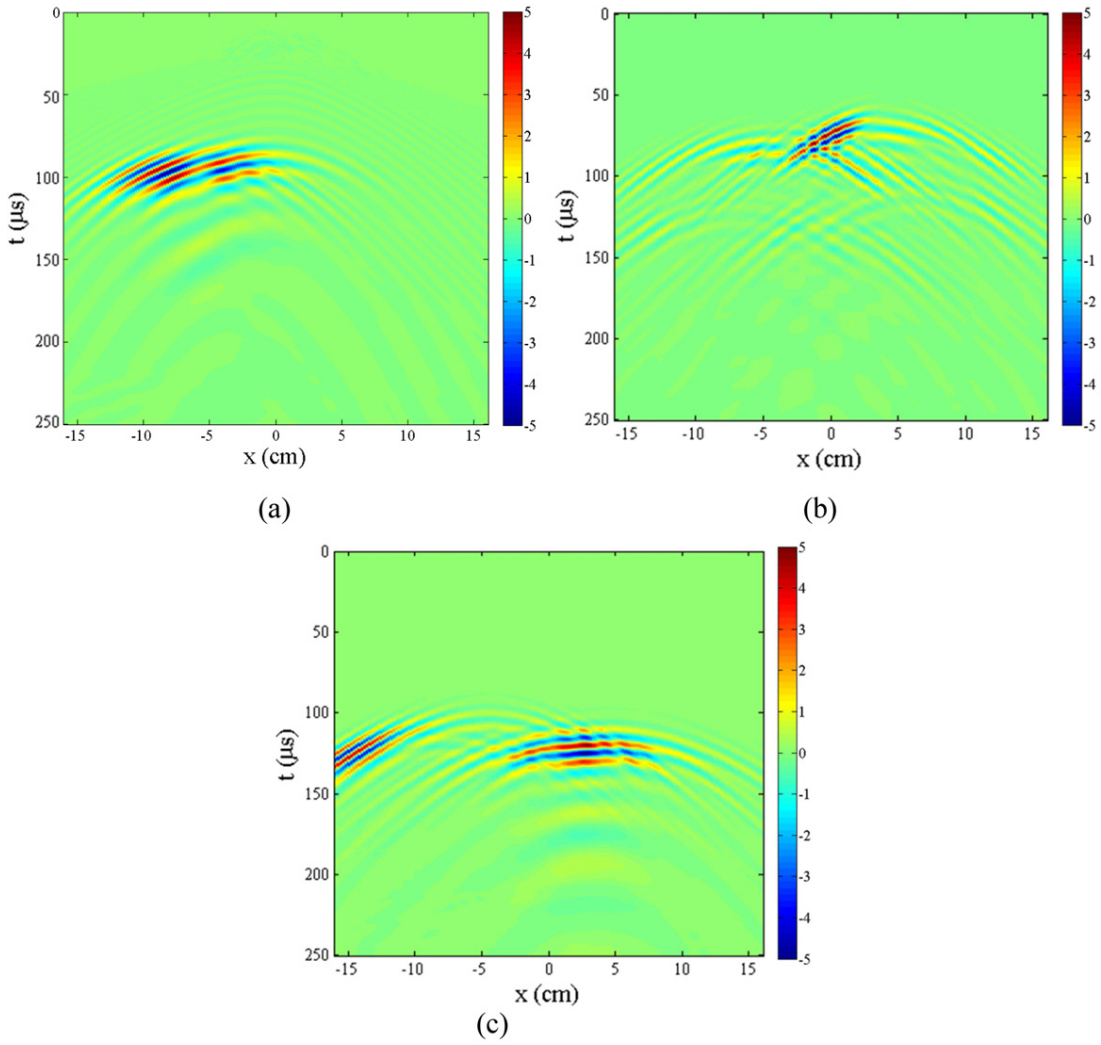

Figure 3. Time sections of synthetic scattered wavefields for different damage cases. (a) Case I. (b) Case II. (c) Case III.

a small region of the plate with reduced material constants. The boundary conditions at the interfaces between the plate and damage are implicitly satisfied, which makes it easier to model damage with complicated geometries and material properties. In this study, two types of damage are considered: one is a rectangular-shaped crack with the bending stiffness D at the grid points representing the crack chosen to have $1/16$ of the normal plate's bending stiffness; the other type is a circular shaped damage site with $1/4$ of the normal plate's bending stiffness [24].

The size of the aluminum plate studied is 40 cm × 40 cm. A 200 × 200 FD mesh with a uniform square grid space $\Delta x = \Delta y = 0.2$ cm is superimposed on the plate region. The time step for the calculation is set as 0.0625 μs. The spatial and time discretizations are chosen to ensure minimum grid dispersion and numerical stability. The total time span is 250 μs with 4000 time steps. The origin of the coordinate system is set at the center of the plate, the x axis is along the horizontal direction and the y axis is along the vertical direction. In the numerical simulation section, a linear sensor array with 161 PZT wafers located at $y = 0$ and -16 cm $\leq x \leq 16$ cm with the same spacing as the FD grid is used. Three damage cases are considered. Case I: a single 6 cm × 0.5 cm crack of rectangular shape is centered at $(-3, -8)$ cm. Case II: double circular shaped damage points with the same radius of 1.6 cm are centered at $(-5, -8)$ cm and $(4, -7)$ cm, respectively. Case III: double cracks of rectangular shape with sizes of 3 cm × 0.5 cm and 6 cm × 0.5 cm are centered at $(-8.5, -10)$ cm and $(4, -13)$ cm, respectively. In practical applications, the spacing of the sensor network is much bigger; an interpolation method could be employed to reconstruct the scattered wavefield with denser sensing locations to increase the quality of the final images [26]. In the study, it is assumed that the size of the PZT wafer is sufficiently small such that it can be neglected and the transfer function between the structure and the wafer is not considered.

For all three cases, the actuator is subjected to a narrowband tone burst excitation described by

$$Q(t) = P[H(t) - H(t - 2\pi N_{\mathrm{p}}/\omega_0)] \times [1 - \cos(\omega_0 t/N_{\mathrm{p}})]\sin(\omega_0 t) \quad (13)$$

where P is the amplitude of the excitation force, $H(t)$ is the Heaviside step function, N_{p} is the number of peaks of the

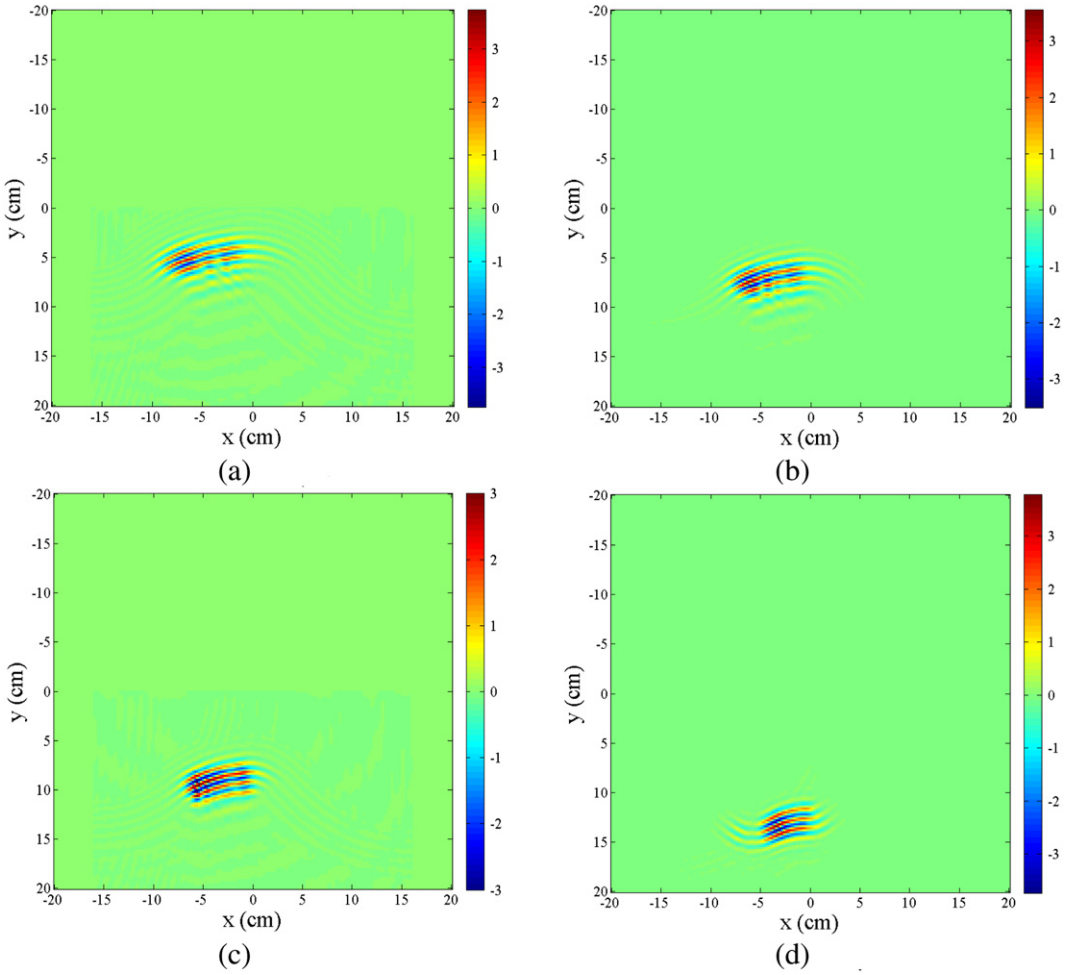

Figure 4. Snapshots of back-propagation of the scattered wavefield in the spatial section at different times for Case I. (a) 70 μs, (b) 50 μs, (c) 30 μs and (d) 10 μs.

signal, and ω_0 is the center angular frequency of the signal. Applying the spatial Fourier transform to the excitation, we have $Q(\omega) = \frac{\mathrm{i}\omega_0^2 P}{N_\mathrm{p}^2(\omega_0-\omega)^3-(\omega_0-\omega)\omega_0^2}[\mathrm{e}^{\frac{\mathrm{i}2\pi(\omega_0-\omega)N_\mathrm{p}}{\omega_0}} - 1]$. Based on Mindlin theory, the incident wavefield for the current excitation can be calculated as [25]:

$$W^\mathrm{i}(r,\omega) = \frac{\mathrm{i}BQ(\omega)}{4\rho h\omega^2(k_1^2+k_2^2)} \times [H_0^{(2)}(k_1 r) - H_0^{(2)}(-\mathrm{i}k_2 r)] \qquad (14)$$

where $Q(\omega)$ is the Fourier transform of the applied transverse point load $Q(t)$, $H_0^{(2)}$ is the zero-order Hankel function of the second kind, $r = \sqrt{(x-x_\mathrm{e})^2+(y-y_\mathrm{e})^2}$ is the propagating distance from the excitation point $(x_\mathrm{e}, y_\mathrm{e})$.

Figure 3 shows the time sections of synthetic scattered wavefields with different damage cases when PZT at (0, 0) cm is actuated. In the figure, the abscissa represents the position of sensors deployed along the central horizontal axis ($y = 0$) of the plate. The ordinate represents the propagating time of the waves. In this study, the parameters are selected as: $P = 1$ N, $N_\mathrm{p} = 3$ and $f_0 = \omega_0/2\pi = 150$ kHz. Notice that the excitation frequency is well below the cut-off frequency, therefore only the first mode of the flexural wave is actuated. The scattered wavefields from the damage are obtained by subtracting the wavefields without damage from the total wavefields of the plate with damage. Sensor array data collected from the scattered wavefields are assembled into the form of time sections.

3.2. Results of damage imaging

The aim of the time-reversal process is to transfer the wave data of the sensor array in the time section to its source in the spatial section. Applying the proposed time-reversal process in the f–k domain to the time sections of the scattered wavefields as illustrated in figure 3 and performing inverse temporal Fourier transform to $W^\mathrm{s}(x, y, \omega)$, the information about the damage—namely the sources of the scattered waves—can be obtained in the spatial domain. Figure 4 shows snapshots of the back-propagation of the scattered wavefield in the spatial section at four different times for damage Case I. From the figures, it can be clearly seen that recorded scattered wavefields at $y = 0$ by the linear sensor array are successfully back-propagated toward the damage. However, though it can be deduced from these figures that the times when the scattered wavefield propagates back to the damage

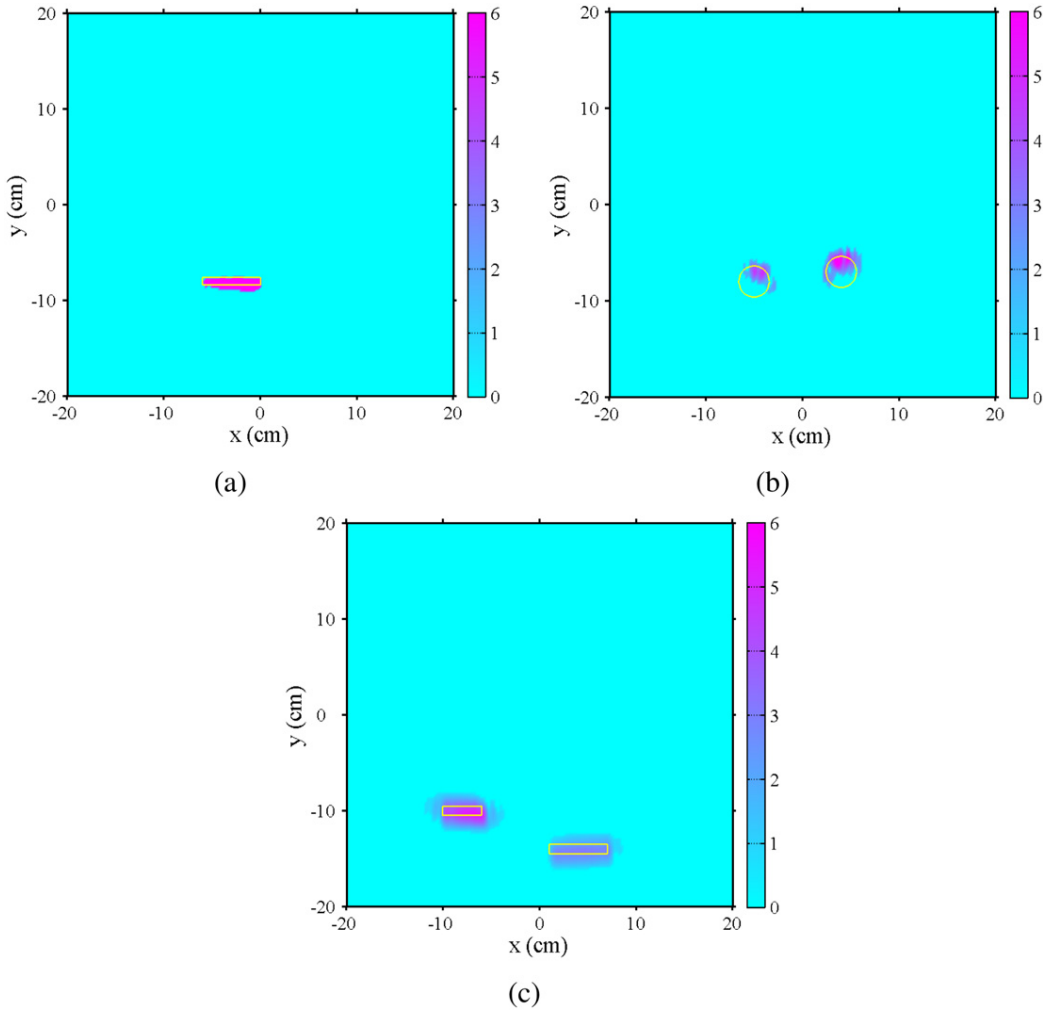

Figure 5. Damage images obtained by using the proposed time-reversal technique in the f–k domain. (a) Case I, (b) Case II. (c) Case III.

are between 30 and 50 μs, it cannot be exactly known and will be determined by the imaging condition.

Instead of using the back-propagated scattered wavefield in the time domain, a cross-correlation imaging condition between the back-propagated scattered wavefield and incident wavefield is employed in the frequency domain. Figure 5 shows the generated damage images using the cross-correlation imaging condition. The actual simulated damage is also highlighted by yellow lines for comparison. To increase the fidelity of the resulting images, the same excitation signal is applied to different actuators, which are at (−4, 0), (0, 0) and (4, 0) cm, to produce multiple damage images which are then superimposed to generate the final image result. By performing the stacking, the final image resolution of the damage can be enhanced. For a single rectangular crack, the damage image agrees well with the actual position and length of the crack, as shown in figure 5(a). For circular shaped damage, similar results are obtained. The damage image in figure 5(b) shows they are mainly located around the upper boundaries of the actual simulated damage, which is understandable since the excitation point is placed above the damage and the scattered waves are mainly reflected from the upper boundaries. Although the image is not very sharp, the image result obtained by using the proposed time-reversal technique clearly displays the arc shape of the circular damage. The lower portions of the circular damage images can be improved by simply placing another sensor array under the two damage sites. A very accurate image result is also found for the case of two rectangular cracks, as shown in figure 5(c). Therefore, the proposed technique has the capability of not only localizing multiple damage sites but also identifying their extents.

One significant advantage of the proposed time-reversal technique in the f–k domain for damage imaging is that it significantly increases the speed of damage detection and imaging. By employing the algorithm of the fast Fourier transform 'FFT', the damage can be imaged in near real time. The process of back-propagating the scattered wave and imaging the damage for a 40 cm × 40 cm plate with 200 pixels × 200 pixels takes no more than 40 s on a PC with a Intel P4 3.0 GHz CPU and 6 GB memory. This is about two orders faster than the existing time-reversal technique used for damage identification in the time domain. Using a compilable computer language, such as the C language, or implementing the routines on a specific hardware device, such as a digital signal processor (DSP), the total execution

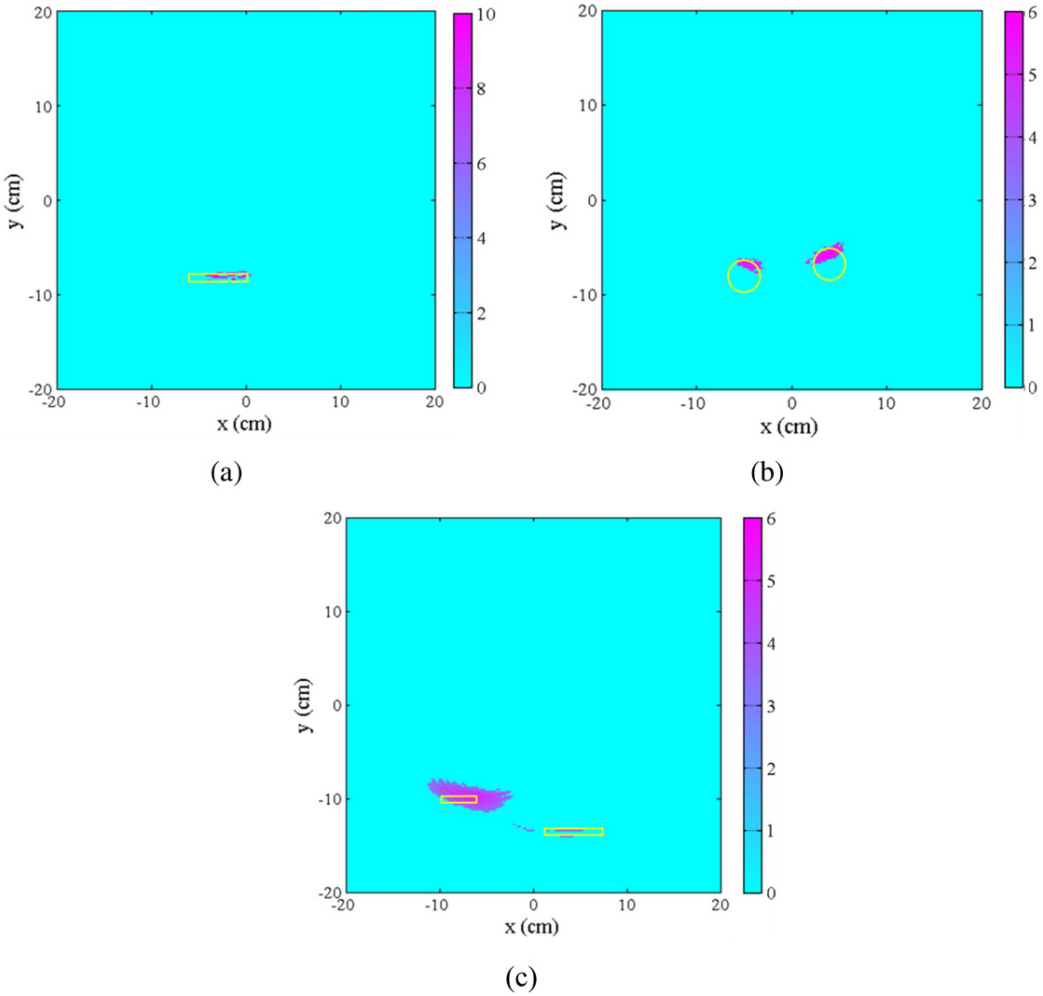

Figure 6. Damage images obtained by using the delay–sum approach. (a) Case I. (b) Case II. (c) Case III.

time can be drastically reduced, meeting the requirement of damage identification for an on-line SHM system.

Finally, imaging results from the proposed f–k domain time-reversal technique are compared with those from the conventional delay–sum approach. The basic idea of the approach is first to 'delay' and then to 'sum' received sensor signals according to the calculated TOF of a signal traveling from the actuator to one image point (grid) and on to the sensor. Therefore, the delay–sum approach is also comparably efficient in time. To simplify comparisons, a minimally dispersive propagating wave is assumed for the calculation of a simple time-shift. This assumption is reasonable for narrowband signals with little dispersion. The same linear sensor array with PZT wafers is used and the same excitation signal is applied to the three actuators alternatively, as mentioned previously. If there is damage located at the point $(x_m,\ y_n)$, then the total TOF of the actuator–sensor pair (i, j) is

$$t_{ij}(x_m,\ y_n) = \left\{\sqrt{(x_m - x_i)^2 + (y_n - y_i)^2} + \sqrt{(x_m - x_j)^2 + (y_n - y_j)^2}\right\}\{c_g\}^{-1} + \Delta t_b \tag{15}$$

where $(x_i,\ y_i)$ and $(x_j,\ y_j)$ are the coordinates of the actuator and sensor, respectively, c_g is the group velocity associated with the center frequency of the narrowband tone burst excitation signal, Δt_b denotes half the duration of the excitation signal. The pixel value at each image point is constructed from the summation of the signal of every actuator–sensor pair as

$$\bar{I}(x_m,\ y_n) = \sum_{i=1}^{3}\sum_{j=1}^{\bar{n}} w^s(x_m,\ y_n, t_{ij}(x_m,\ y_n)) \tag{16}$$

where $\bar{n}$ is the number of the PZTs, and the weighting factor is chosen as one [15]. Figure 6 shows the image constructed from the sensor signals of scattered waves based on the delay–sum approach. For the single rectangular-shaped crack, comparison between figures 5(a) and 6(a) shows that the delay–sum approach can capture the location of the crack but the size of the crack cannot be precisely quantified. For circular shaped damage, both image results in figures 5(b) and 6(b) illustrate imaging areas mainly located around the upper boundaries of the circular damage, however, no clear arc shape can be detected by using the delay–sum approach. For multiple cracks, as shown in figure 6(c), the delay–sum approach cannot provide good quantitative information on both cracks,

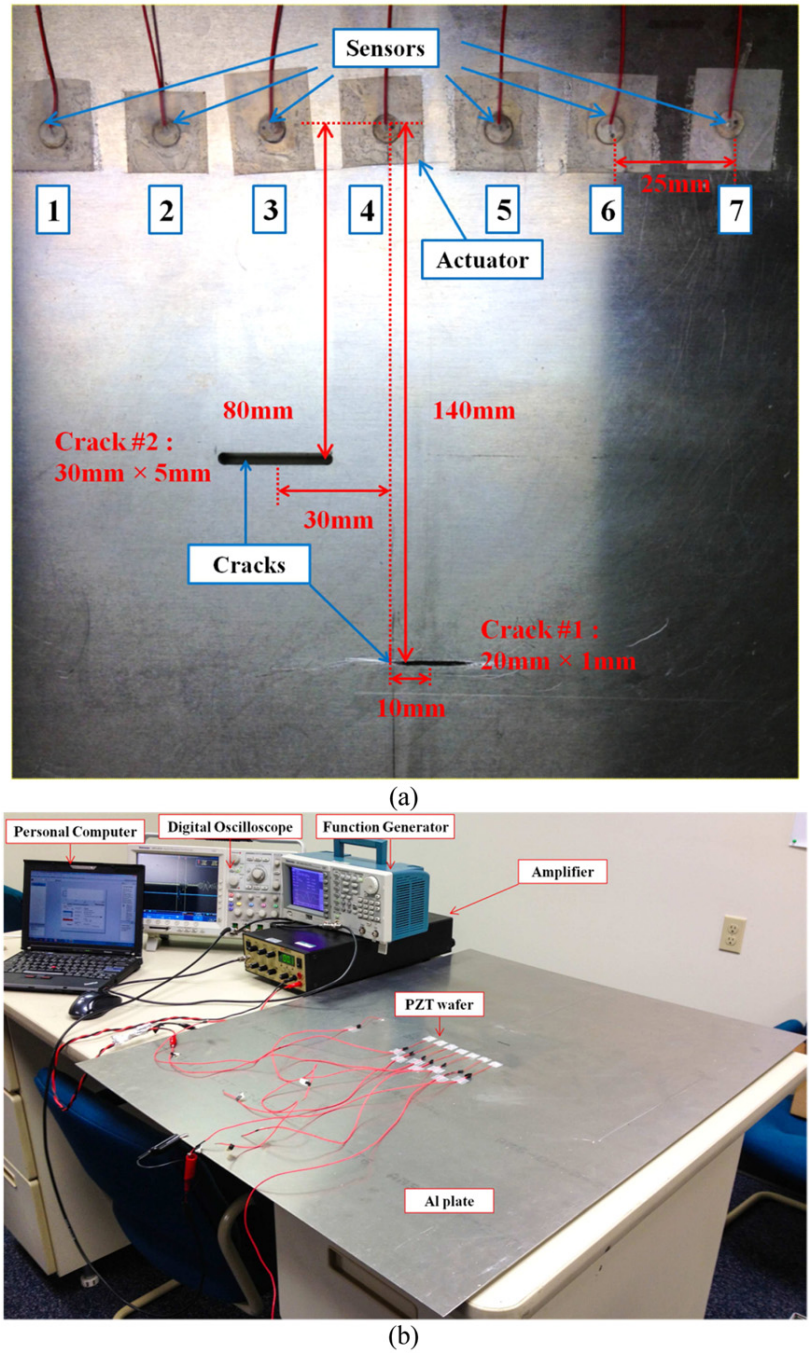

Figure 7. (a) The layout of the PZT sensor/actuators array and the cracks. (b) The experimental setup.

especially for the crack in the distant right location. This can be attributed to the fact that the imaging loci of the multiple cracks after summation could affect the final image of the cracks. In conclusion, in comparison with the conventional delay–sum approach, the proposal time-reversal technique can provide more accurate quantitative information about the damage, including the position, size and shape. It is expected since the time-reversal technique can recover the entire back-propagated scattered wavefield, which accurately captures information about the sizes and shapes of the damage. The delay–sum approach is mostly based on the received single-frequency signals, therefore the delay process cannot recover the real amplitude information of the waves scattered by the damage. Another advantage of the time-reversal technique is that the approach does not require a large number of sensor signals, as illustrated in the following experimental testing.

4. Experimental validation

In this section, experimental work is pursued to validate the feasibility of applying the proposed technique for fast identification of multiple damage. The experimental configuration for an integrated plate with a sparse actuator/sensor network is shown in figure 7(a). An aluminum plate (Type 6061-T6) with a thickness of 0.16 cm is prepared and two rectangular slots

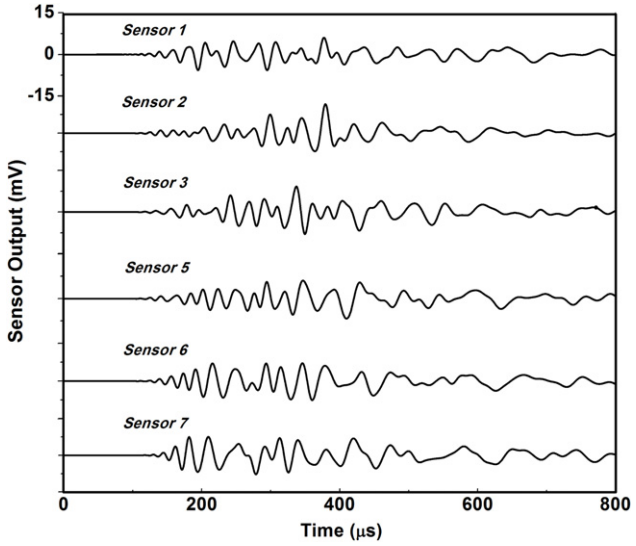

Figure 8. Scattered wave signals recorded by each sensor.

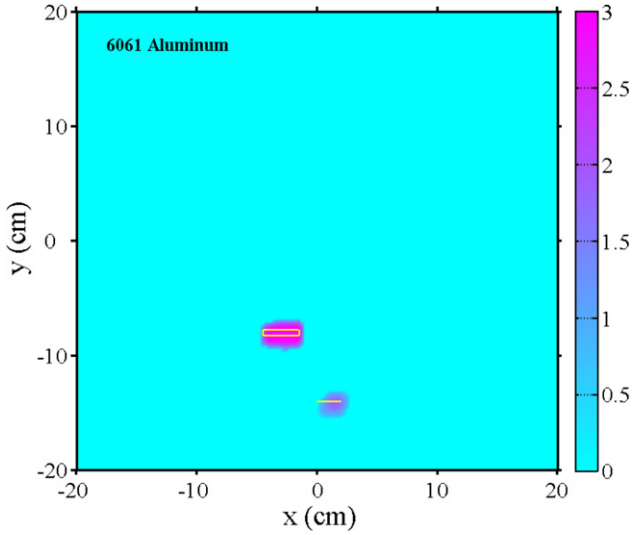

Figure 9. Final image of the multiple cracks from experimental measurements.

are cut through the thickness of the plate to simulate cracks. The origin of the coordinate system is set at the center of the PZT wafer #4, the x axis is along the horizontal direction and the y axis is along the vertical direction. One rectangular slot is 2 cm × 0.1 cm with its center at (1, −14) cm, the other slot is 3 cm × 0.5 cm with its center at (−3, −8) cm. Seven PZT wafers with dimension of 6.1 mm diameter and 0.56 mm thickness (Piezo Kinetics Navy Type II) are mounted on the plate to form a horizontal linear array, with a sensor gap of 2.5 cm and a total sensor span of 15 cm.

The experimental setup is shown in figure 7(b). A 3-peak narrowband tone burst excitation signal is generated by the function generator (Tektronix AFG3021). The central frequency of the excitation is chosen at 300 kHz for two reasons: first, the lowest antisymmetric mode A_0 is dominated; second, the wavelength at this frequency range is comparable to the lengths of the cracks, which can provide suitable image resolution. Then, the input signal is amplified by a wideband power amplifier (Krohn-Hite 7602 M) and drives the PZT wafer #4, which is set to be the actuator to generate plate waves. All the other six PZT wafers function as sensors and the sensor signals are collected by the digital oscilloscope (Tektronix DPO4034) and processed in the personal computer by the software NI SignalExpress in the experiment. The transient signals are digitized with 10 000 points using a sampling frequency of 10 MHz.

Figure 8 gives the sensor signals of the scattered waves excited by PZT wafer #4. The scattered wavefield is obtained by subtracting the sensor signals with cracks from the corresponding sensor signals of the virgin plate. It should be noticed that the 3-peak shape of the excitation signal cannot be clearly observed in the recorded signals, which may be caused by wave dispersion, wave mode conversion and multiple reflections between the two cracks. The A_0 mode is dominant, followed by the continuous wave signals corresponding to another converted S_0 propagation mode, having a different propagation velocity. Other interval signals are not significant, probably due to multiple reflections between the two cracks. In addition, the amplitude varies greatly among traces without a clear pattern, which is caused by the different strength and thickness of the adhesive layer for PZT wafers bonded on the surface of the aluminum plate.

In order to not only obtain the location information but also obtain the geometry of the crack, an array with enough sensor signals is necessary in the reversal wave technique. In order to do this, an interpolation based on the acquired data from the six sensors is applied to construct a complete time section that covers all grid points in the space between PZT wafer #1 and PZT wafer #7. In this study, a 40 cm × 40 cm plate area with 400 × 400 spatial discretization is analyzed for the time-reversal process. The whole reflection wavefield is reconstructed in two dimensions (one dimension in time and the other in space) using a polynomial curve fitting through solving the least-squares problem. Better resolution of the damage image can be expected after the interpolation process. Applying the proposed time-reversal process to the time section of the experimentally measured scattered waves in the f–k domain along with the cross-correlation imaging condition discussed in section 2, the damage image can be obtained. Applying the stacked damage images from all seven actuators, the final experimental image result with enhanced SNR can be obtained, as shown in figure 9. From the figure, the location and length of the larger crack (3 cm × 0.5 cm) can be quantitatively identified. For the small crack (2 cm × 0.1 cm), its location and length information is also identified, although the image of the small crack is a little blurry. This can be attributed to the fact that part of the scattered waves from the small crack are blocked by the large crack and most of the information about the small crack is contained only in PZT wafers# 1–4, therefore the clarity of the damage image of the small crack is low compared with that of the large crack. However, the experimental result does demonstrate the feasibility of detecting damage by applying the fast time-reversal technique. It should be noticed that the image resolution and quantification of the damage can be

further improved by increasing the density of the sensors or the wave frequency.

5. Conclusions

This paper proposes a time-reversal technique in the frequency–wavenumber domain for fast detection of plate damage using scattered flexural plate waves. Based on Mindlin plate theory, the time-reversal process for the lowest antisymmetric flexural plate wave is developed in the f–k domain. By using the cross-correlation imaging condition in the frequency domain, damage images can be quantitatively obtained. Numerical simulation studies on synthetic scattered wavefields demonstrate that the proposed technique has the capability of not only localizing multiple damage but also identifying its extent. Moreover, the technique developed in this study is about two orders of magnitude faster than the time-reversal method in the time domain. Finally, experimental testing is conducted to validate that the proposed technique is a useful tool for fast damage detection and identification in an on-line SHM system.

References

[1] Sohn H, Farrar C R, Hemez F M, Shunk D D, Stinemates D W, Nadler B R and Czarnecki J J 2003 A review of structural health monitoring literature: 1996–2001 *Los Alamos National Laboratory Report* LA-13976-MS (Los Alamos, NM)

[2] Huang G L, Song F and Wang X D 2010 Quantitative modeling of coupled piezo-elastodynamic behavior of piezoelectric actuators bonded to an elastic medium for structural health monitoring: a review *Sensors* **10** 3681–702

[3] Su Z, Ye L and Lu Y 2006 Guided Lamb waves for identification of damage in composite structures: a review *J. Sound Vib.* **295** 753–80

[4] Zou Y, Tong L and Steven G P 2000 Vibration-based model-dependent damage(delamination) identification and health monitoring for composite structures—a review *J. Sound Vib.* **230** 357–78

[5] Roh Y S 1998 Built-in diagnostics for identifying an anomaly in plates using wave scattering *PhD Dissertation* Stanford University

[6] Cawley P and Alleyne D 1996 The use of Lamb waves for the long range inspection of large structures *Ultrasonics* **34** 287–90

[7] Guo N and Cawley P 1994 The interaction of Lamb waves with delaminations in composite laminates *J. Acoust. Soc. Am.* **94** 2240–6

[8] Valdes S H and Soutis C 2002 Real-time nondestructive evaluation of fiber composite laminates using low-frequency Lamb waves *J. Acoust. Soc. Am.* **111** 2026–33

[9] Lemistre M and Balageas D L 2001 Structural health monitoring system based on diffracted Lamb wave analysis by multiresolution processing *Smart Mater. Struct.* **10** 504–11

[10] Song F, Huang G L and Hudson K 2009 Guided wave propagation in honeycomb sandwich structures using a piezoelectric actuator/sensor system *Smart Mater. Struct.* **18** 125007

[11] Su Z, Ye L and Bu X 2002 A damage identification technique for CF/EP composite laminates using distributed piezoelectric transducers *Compos. Struct.* **57** 465–71

[12] Michales J E and Michaels T E 2007 Guided wave signal processing and imaging fusion for *in situ* damage localization in plates *Wave Motion* **44** 482–92

[13] Ihn J B and Chang F K 2008 Pitch-catch active sensing methods in SHM for aircraft structures *Struct. Health Monit.* **7** 5–19

[14] Giurgiutiu V and Bao J 2004 Embedded-ultrasonics structural radar for *in situ* structural health monitoring of thin-wall structures *Struct. Health Monit.* **3** 121–40

[15] Yu L and Giurgiutiu V 2007 *In situ* optimized phased arrays for Lamb wave structural health monitoring *J. Mech. Mater. Struct.* **2** 459–91

[16] Quaegebeur N, Masson P, Langlois-Demers D and Micheau P 2011 Dispersion-based imaging for structural health monitoring using sparse and compact arrays *Smart Mater. Struct.* **20** 025005

[17] Raghavan A and Cesnik C E S 2007 Review of guided-wave structural health monitoring *Shock Vib. Dig.* **39** 91–114

[18] Ing R and Fink M 1998 Time-reversed Lamb waves *IEEE Trans. Ultrason. Ferroelectr. Freq. Control* **45** 1032–43

[19] Ing R and Fink M 1996 Time recompression of dispersive Lamb waves using a time reversal mirror-application to flaw detection in thin plates *Proc. Ultrason. Symp.* **1** 659–63

[20] Park H W, Sohn H, Law K H and Farrar C R 2007 Time reversal active sensing for health monitoring of a composite plate *J. Sound Vib.* **302** 50–66

[21] Sohn H, Park H W, Law K H and Farrar C R 2007 Damage detection in composite plates by using an enhanced time reversal method *J. Aerosp. Eng.* **20** 141–51

[22] Sohn H, Park H W, Law K H and Farrar C R 2007 Combination of a time reversal process and a consecutive outlier analysis for baseline-free damage diagnosis *J. Intell. Mater. Syst. Struct.* **18** 335–46

[23] Wang X D and Huang G L 2004 Evaluation of cracks in elastic media using surface signals *Int. J. Mech. Mater. Des.* **1** 383–98

[24] Lin X and Yuan F G 2001 Damage detection of a plate using migration technique *J. Intell. Mater. Syst. Struct.* **12** 469–82

[25] Lin X and Yuan F G 2001 Detection of multiple damages by prestack reverse-time migration *AIAA J.* **39** 2206–15

[26] Lin X and Yuan F G 2005 Experimental study applying a migration technique in structural health monitoring *Struct. Health Monit.* **4** 341–53

[27] Ruzzene M 2007 Frequency–wavenumber domain filtering for improved damage visualization *Smart Mater. Struct.* **16** 2116–29

[28] An Y K, Park B and Sohn H 2013 Complete noncontact laser ultrasonic imaging for automated crack visualization in a plate *Smart Mater. Struct.* **22** 025022

[29] Mindlin R D 1951 Influence of rotary inertia and shear on flexural motions of isotropic elastic plates *J. Appl. Mech.* **18** 31–8

[30] Rose L R F and Wang C H 2004 Mindlin plate theory for damage detection I: source solutions *J. Acoust. Soc. Am.* **116** 154–71

[31] Liu F Q, Hanson D W, Whitemore N D, Day R S and Stolt R H 2006 Toward a unified analysis for source plane-wave migration *Geophysics* **71** S129–39